$ZnFe_2O_4$ nanoparticles: synthesis, characterization, and enhanced gas sensing property for acetone

Jie Zhang, Ji-Ming Song*, He-Lin Niu, Chang-Jie Mao, Sheng-Yi Zhang, and Yu-Hua Shen

School of Chemistry & Chemical Engineering, Key Laboratory of Functional Inorganic Materials Chemistry of Anhui Province, Anhui University, Hefei, Anhui, 230601, P. R. China.

Tel*:+86 0551 63861279* : Fax*: +86 0551 63861279*

E-mail: jiming@ahu.edu.cn

Abstract

$ZnFe_2O_4$ nanoparticles with diameter of ca.10 nm were successfully synthesized under hydrothermal conditions without using any surfactant or structure-directing agents. The structure, composition and morphology of the samples were characterized by means of powder X-ray diffraction (XRD), X-ray photoelectron spectroscopy (XPS), field-emission scanning electron microscopy (SEM), transmission electron microscopy (TEM), diffuse reflectance spectra (DRS) and the Brunauer-Emmett-Teller (BET) surface area measurement. The results showed that the mole ratio of reactants ZnO to $FeCl_3$ played an important role in controlling the composition and morphology of the products. BET specific surface area of $ZnFe_2O_4$ nanoparticles was evaluated to be 115.6 $m^2 g^{-1}$. Interestingly, as-prepared $ZnFe_2O_4$ nanoparticles displayed enhanced gas sensing performance to acetone, which response value reached 39.5 for 200 ppm acetone gas at lower optimum working temperature of 200 ºC, in comparison with the precursor ZnO (4.2) at the same condition. The gas sensing property demonstrates that as-prepared $ZnFe_2O_4$ has potential applications in the detection of acetone.

Key words: $ZnFe_2O_4$; nanoparticles; gas sensor; acetone

1. Introduction

Spinel oxides (AB_2O_4) have been known for a long time for their interesting electronic and magnetic properties and are thus suitable for various industrial applications, ranging from magnetic cores and high-frequency devices to medical diagnostic and environment monitoring [1,2]. Among them, ferrite, an iron oxide-based mixed metal oxide, has been extensively studied due to its unique properties [3]. As a typical ferrite spinel (AFe_2O_4; A=Mn, Zn, Co, Ni, Cd), zinc ferrite ($ZnFe_2O_4$) has received great interests due to its significant applications in photocatalysis, information storage, electronic devices, magnetic materials and gas sensing [4,5]. In recent years, many efforts have been devoted to synthesize $ZnFe_2O_4$ nanomaterials. $ZnFe_2O_4$ nanomaterials with different morphologies, such as nanoparticles [6], nanorods [7], core-shell microsheres [8], nanotube [9], thin film [10] et al. have been prepared. Synthesis techniques include co-precipitation, template method, sol-gel reaction, solvothermal route and so on. Yasuki et al. have prepared zinc ferrite-based xerogel monoliths via a sol-gel route [11]. Darshane et al. have synthesized zinc ferrite nanoparticles at 700^{o}C using sodium chloride as growth inhibitor [12]. Hydrothermal method has proved an effective way to synthesize nanomaterials with controllable nanostructure and useful properties. Rahman et al. have synthesized $ZnFe_2O_4$ nanorods with efficient chemical sensor application [13]. Xia et al. have synthesized $ZnFe_2O_4$/graphene composites and studied their application for lithium-ion batteries [14]. Mueller et al. have reported the electrochemical performance of $ZnFe_2O_4$ nanoparticles [15]. Sun et al. have prepared

$ZnFe_2O_4$ octahedra and discussed its photocatalytic activities [16].

Spinel oxides (AB_2O_4) were found to be more attractive than single-metal oxides for their better response to certain gases [17]. The gas sensing properties of $ZnFe_2O_4$ are different and sensitive according to the preparation methodology or synthesis parameters of samples. This is due to the fact that their microstructure and oxygen vacancies are responsible for the sensing property. Recently, Patil et al. have synthesized single phase nanocrystalline $ZnFe_2O_4$ with size of 25-30 nm and tested their gas response to acetone and liquefied petroleum gas [18]. Sutka et al. have obtained $ZnFe_2O_4$ thin film gas sensors for the detection of ethanol with low response and fast response and recovery behavior [10]. Cao et al. have synthesized $ZnFe_2O_4$ nanomaterials, which exhibited efficient gas sensing properties for ethanol and hydrogen sulfide [19]. To our knowledge, the synthesis of well-dispersed $ZnFe_2O_4$ nanoparticles with high performance gas sensing property for acetone has rarely been reported.

Herein, we report the synthesis of magnetic $ZnFe_2O_4$ nanoparticles with diameter size of ca.10 nm by using hydrothermal method. Morphologies, structure, BET, and magnetic properties of as-prepared samples have been characterized or measured. The suitable reaction conditions, such as the reactant mole ratio, reaction temperature and time have been explored. In addition, $ZnFe_2O_4$-based gas sensors have been used to test some common compounds, for instance, acetone, ethanol, methanol, isopropanol, ethyl acetate and methanal. The results display that the gas sensor has superior response for detecting of acetone gas to that of other compounds.

2. Experimental

2.1. Chemicals

The zinc chloride ($ZnCl_2$), sodium borohydride ($NaBH_4$, 96% wt%), silver nitrate ($AgNO_3$), anhydrous ferric chloride ($FeCl_3$), L-ascorbic acid and hydrazine hydrate (85% v/v%) were applied in our experiment. All chemicals are of analytical grade and used as received, without any further purification.

2.2 Synthesis of $ZnFe_2O_4$ nanoparticles

A typical procedure for the synthesis of $ZnFe_2O_4$ included two steps:

(1) Synthesis of ZnO

Shuttle-like ZnO nanoparticles were synthesized based on our previous work [20]. Briefly，80 mL distilled water was added into a three-necked flask with capacity of 100 mL, and heated to 80 ^oC, then 0.8 mmol (0.109 g) $ZnCl_2$ and 4 mmol (0.151 g) $NaBH_4$ were added into the flask with vigorous magnetic stirring. After 2 h, the white product was obtained by centrifuging the final reaction mixture with distilled water and ethanol several times each, and then dried at 60 ^oC for 6 h for further experiment.

(2) Synthesis of $ZnFe_2O_4$

A 4 mL aqueous dispersion containing 0.024 g of freshly prepared ZnO was homogeneously mixed with 0.097 g $FeCl_3$ and 0.053 g ascorbic acid by ultrasonication for 30 s. Then, 1 mL of hydrazine hydrate was added into the above dispersion to form a homogeneous dark solution with magnetic stirring for about 20 min. After that, the mixed solution was transferred and sealed into a 10 mL Teflon-lined stainless steel autoclave, heated at 180 ^oC in an electric oven for 12 h,

then cooled to room temperature naturally. The black products were obtained by centrifuging and washing the final precipitation with distilled water and ethanol several times each, and then dried at 60 ºC for 6 h for further characterization. The comparison tests followed same reaction procedures as the above description except for a given parameter.

2.3 Instruments and characterization

The samples were characterized by different analytic techniques. Powder X-Ray diffraction (XRD) was obtained on a Rigaku D/max-RA X-ray diffractometer with CuKα1 radiation (λ=0.15406 nm). Scanning electron microscopy (SEM) images were performed on a Hitachi S4800 microscopy operating at 5.0 kV. The transmission electron microscopy (TEM) images, high resolution TEM (HRTEM) observation and selected area electron diffraction (SAED) were carried out on a JEOL-2100 TEM with an acceleration voltage of 200 kV. The specific surface area was calculated by the Brunauer-Emmett-Teller (BET) method and the mesopore size distribution was calculated by Barrett-Joyner-Halenda (BJH) method. X-ray photoelectron spectroscopy (XPS) was performed by using a VG ESCA scientific theta probe spectrometer in constant analyzer energy mode with a pass energy of 28 eV and AlKα (1486.6 eV) radiation as the excitation source. Magnetic measurements were carried out at room temperature using physical property measurement system (PPMS, EC-II (9T)) with a maximum magnetic field of ±5 kOe. UV-vis spectrometer (Shimadzu UV-3600 PC) was used to record diffuse reflectance spectra of as-prepared samples at room temperature using $BaSO_4$ as a reference.

2.4 Fabrication of gas sensors and gas sensing detection

The WS-30A static gas-sensing system (Weisheng Electronics Co. Ltd., Zhengzhou, China) was used to examine the sensing performance of the sensors.

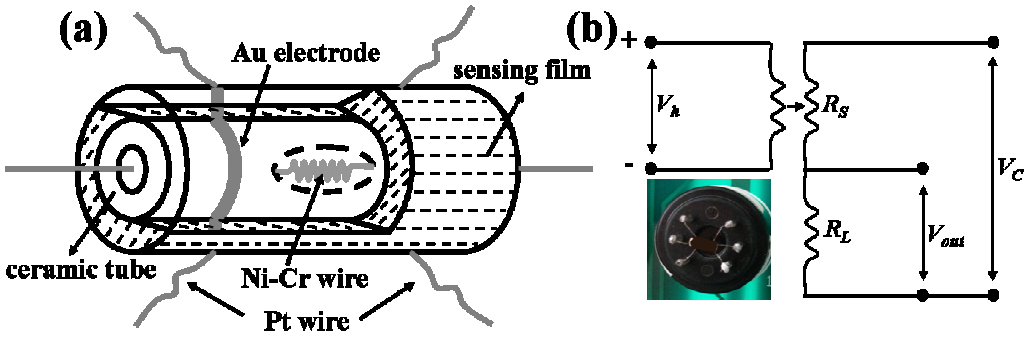

Fig. 1. Schematic of the gas sensor structure (a) and the measuring electric circuit of gas sensor (b). The inset in (b) is a photograph of as-prepared sensor.

Fig. 1 showed the structure schematic of sensor and the fabricating procedure of a typical $ZnFe_2O_4$-based gas sensor. First, $ZnFe_2O_4$ powders were mixed with deionized water to form a paste. The paste was coated on the surface of the ceramic tube and dried in air. Then the electrodes were welded on the basement. A Ni-Cr heating wire crossing the ceramic tube, which was used to control the operating temperature, was also welded on the basement. (Detail information can be found in Fig. S1 in the ESI). Finally, to improve their stability, the gas sensors were kept at working temperature of 300 ^oC for 5 days. For the measuring electric circuit in Scheme 1(b), the working temperature could be controlled by adjusting the heating voltage (V_h) of the sensor. A load resistor (R_L=1 MΩ) was connected in series with the gas sensor and the gas-sensor performance was obtained from the output voltage (V_{out}) of R_L. The circuit voltage (V_c) is 5 V and the sensor resistance (R_s) can be calculated according to the formula: $R_s=R_L(V_c-V_{out})/V_{out}$. The response ($S$) is defined as $S=R_a/R_g$, where R_a is the

resistance in the air while R_g is the resistance in the mixture gas between air and detected gas.

2.5 Gas preparation methods

In the gas sensing system, the test gases were come from liquid evaporation. To get a certain concentration of gases, a given amount of the test liquid should be injected into a closed chamber with an evaporation device by a micro-syringe. The gas concentration could be controlled by the volume of the test liquid.

The required concentration of the test gases was obtained by the static liquid gas distribution method, which was calculated by the following equation:

$$V_x = \frac{V \times C \times M}{22.4 \times d \times p} \times 10^{-9} \times \frac{273 + Tr}{273 + Tb} \qquad (1)$$

Where *Vx* (mL) is the volume of liquid, *V* (mL) is the volume of test chamber; *C* (ppm) is the gas concentration; *M* (g/mol) is molecular weight of the liquid; *d* (g/cm^3) is the specific gravity of liquid; *p* (%) is purity; *Tr* (^{o}C) is room temperature; *Tb* (^{o}C) is the temperature of test chamber. ”

3. Results and discussion

3.1. Synthesis and characterization

3.1.1. Composition and morphology

The as-prepared nanomaterials were obtained via two step methods under hydrothermal conditions without using any surfactant or structure-directing agents. The composition and crystal phase purity of as-synthesized product were first analyzed by XRD. The XRD patterns of the samples were recorded in a 2θ range of 20^o-80^o.

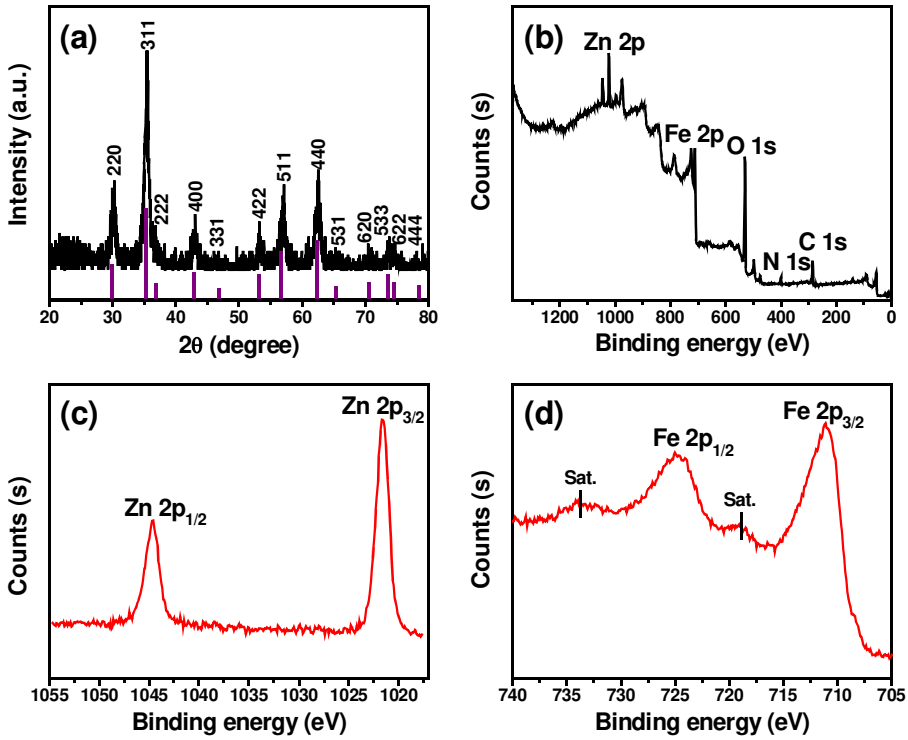

Fig. 2. (a) XRD pattern of the as-synthesized sample and the vertical line at the bottom corresponds to the standard XRD pattern of $ZnFe_2O_4$ (JCPDS No. 22-1012); (b) the XPS survey spectrum of the as-synthesized sample; (c, d) XPS spectra of Zn 2p and Fe 2p, respectively.

Fig. 2(a) shows the typical XRD pattern of the as-prepared samples. All diffraction peaks can be indexed to the phase of $ZnFe_2O_4$ material, which match well with the standard data file of bulk cubic spinel-structured $ZnFe_2O_4$ (JCPDS 22-1012) [21]. No other impurity peaks were detected from the XRD pattern.

XPS survey spectrum of the synthesized samples is shown in Fig. 2(b), which displays the peaks of C 1s (285.3 eV), N 1s (400.1 eV), O 1s (530.7 eV), Fe 2p and Zn 2p. To obtain more information about the samples, we performed high-resolution XPS spectra of Zn and Fe. Fig. 2(c) shows the XPS spectrum of Zn 2p, two peaks centered at 1044.6 eV and 1021.6 eV, which corresponding to the binding energy of Zn $2p_{1/2}$ and Zn $2p_{3/2}$, respectively, indicating the oxidation state of Zn^{2+} in the

samples [22]. Figure 1(d) shows the XPS spectrum of Fe 2p, the main peaks are observed at 725.0 eV and 711.1 eV, which can be assigned to Fe $2p_{1/2}$ and Fe $2p_{3/2}$ respectively. The shoulder peaks at 733.1 and 719.1 eV originating from shakeup process of $2p_{1/2}$ and $2p_{3/2}$ are marked as Sat. in Fig. 2(d), which are evidence to Fe^{3+}[23-25]. The XPS results presented that Zn and Fe elements existed in the synthesized samples were in the forms of Zn^{2+} and Fe^{3+}, respectively, which corresponding to the characterization of the above XRD pattern.

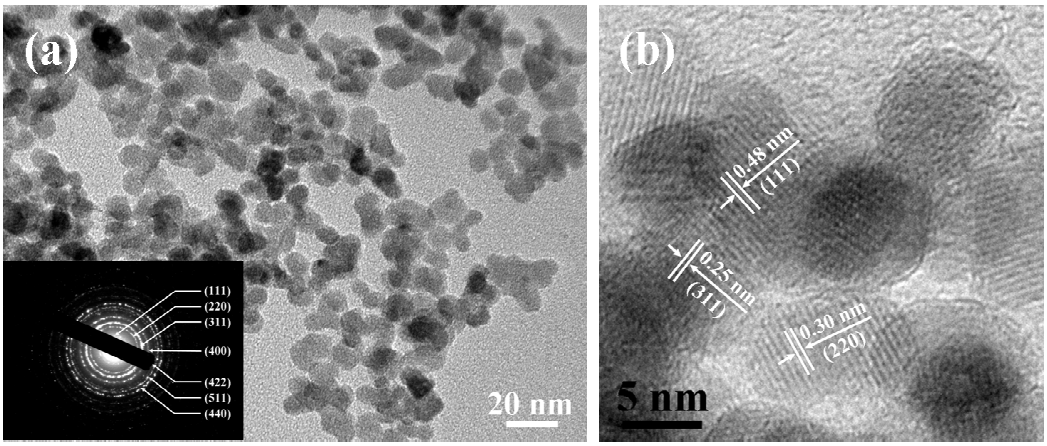

Fig. 3. TEM (a) and HRTEM (b) images of the synthesized sample at 180 ^{o}C for 12 h, the inset in (a) is the corresponding SAED pattern.

The morphology and structure of the samples have been examined by TEM and HRTEM (High resolution TEM). Fig. 3(a) presented that the synthesized samples were composed of well-dispersed particles with average diameter of 10 nm. The inset shows the diffraction spots of SAED pattern for a single particle, which reveals that the as-synthesized samples were polycrystalline with small size nanoparticles. The diffraction rings from inside to outside could be well indexed to (111), (220), (311), (400), (422), (511) and (440) planes, which corresponding to the above XRD pattern. The single nanoparticle displayed clear lattice fringes, suggesting their crystalline

nature in Fig. 3(b). The spacings between neighboring fringes were measured to be 0.48, 0.30 and 0.25 nm, which corresponded to (111), (220) and (311) plane of hexagonal close-packed (*hcp*) $ZnFe_2O_4$ (JCPDS 22-1012) [26].

3.1.2. Optical properties and magnetic measurement of the synthesized samples

The optical properties of the synthesized samples were investigated by UV-visible diffuse reflectance spectra, as shown in Fig. S4. Compared with pure ZnO, the absorption edge of as-prepared $ZnFe_2O_4$ exhibited red-shift trend and presented strong photo-absorption from UV to visible light region [27-29]. The band gap values of ZnO and $ZnFe_2O_4$ were 3.23 eV and 1.86 eV, respectively, corresponding to the reported literature [24]. Room temperature magnetic hysteresis loop of $ZnFe_2O_4$ nanoparticles is shown in Fig. S5. The hysteresis loop showed that saturation magnetization (*Ms*), remanent magnetization (*Mr*), and coercivity (*Hc*) values of the sample were ca. 59.0 emu g^{-1}, 3.0 emu g^{-1} and 37.8 Oe, respectively, so $ZnFe_2O_4$ displayed a paramagnetic behavior [31,32]. The magnetization value at room temperature is obviously higher than the reported $ZnFe_2O_4$ nanomaterials through hydrothermal synthesis [33]. The magnetic nature of the $ZnFe_2O_4$ nanoparticles enables trouble-free separation of the sample from the mixture using an external magnet, which can eliminate the necessity of filtration and centrifugation [34].

3.1.2. BET measurement of the synthesized samples.

Brunauer-Emmett-Teller (BET) measurement has been performed to analyze $ZnFe_2O_4$ nanoparticles. N_2 isotherms as shown in Fig. 4 are close to Type IV curve with an evident hysteresis loop in the 0.45-1.0 range of relative pressure [29,30]. BET

specific surface area of the synthesized sample calculated from N_2 isotherms at 77.5 K was 115.6 m^2g^{-1}. The pore diameter was around 7.4 nm determined by Barrett-Joyner-Halenda (BJH) method (inset in Fig. 4), which was attributed to the interparticle spaces, indicated the mesoporous structure of $ZnFe_2O_4$ nanoparticles. The large specific surface area of $ZnFe_2O_4$ nanoparticles may come from small size of sample, as observed from the TEM images [14]. Compared with precursor ZnO (11.54 m^2g^{-1}) [20], the higher specific surface area of $ZnFe_2O_4$ could provide more efficient active sites, which would enhance the gas sensing performances of $ZnFe_2O_4$ -based sensors.

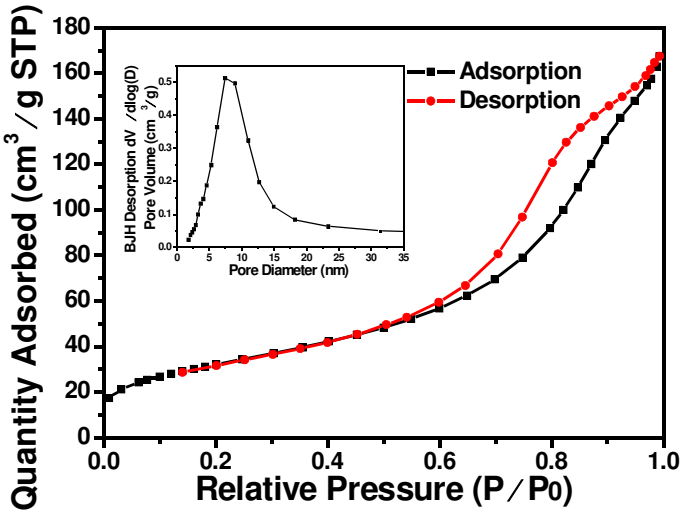

Fig. 4. N_2 adsorption and desorption isotherms of $ZnFe_2O_4$ nanoparticles. The inset is pore-size distribution.

3.1.4. Influence of reaction conditions

Based on a series of control experiments, the results show that the mole ratio of precursor ZnO and $FeCl_3$, reaction temperature and time all played important roles in the composition and phase of samples.

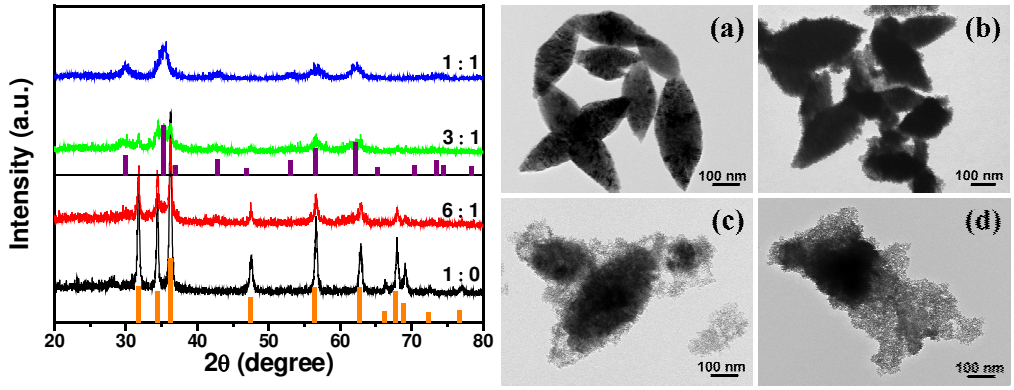

Fig. 5. XRD patterns and TEM images of the sample synthesized with different mole ratios of ZnO to $FeCl_3$: (a) 1:0, (b) 6:1, (c):3:1, (d) 1:1. The yellow line is the standard pattern of ZnO (JCPDS 36-1451) and the purple line is standard pattern of $ZnFe_2O_4$ (JCPDS 22-1012).

The influence of mole ratio of ZnO to $FeCl_3$ has been examined. XRD patterns and TEM images (Fig. 5) show that the products present different compositions and morphologies under different mole ratio of ZnO to $FeCl_3$. When $FeCl_3$ was absented in the reaction system, the obtained samples were shuttle-like ZnO (JCPDS 36-1451). With the mole ratio changed from 6:1 to 1:1, the products were a mixture of ZnO and $ZnFe_2O_4$. The content of $ZnFe_2O_4$ increased gradually with the decrease of mole ratio of ZnO to $FeCl_3$ from XRD patterns, while the shuttle-like morphology of precursor ZnO was destroyed. When the mole ratio was reduced to 1:2, the XRD pattern fitted well with $ZnFe_2O_4$ (JCPDS 22-1012) and no other impurity phases and the morphology was well-dispersed nanoparticles. So the most suitable reactant mole ratio of ZnO to $FeCl_3$ is 1:2 for the synthesis of pure phase $ZnFe_2O_4$ nanoparticles.

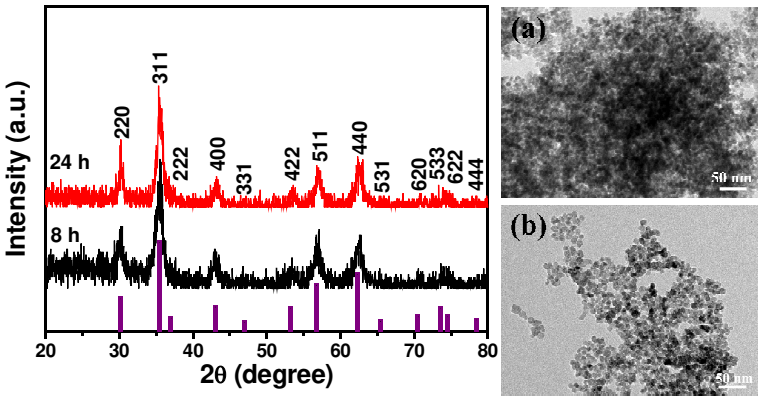

Fig. 6. XRD patterns and TEM images of the samples prepared at 180 ^{o}C with different time: (a) 8 h and (b) 24 h. The vertical line is the standard pattern of $ZnFe_2O_4$ (JCPDS 22-1012).

The influence of reaction time has been discussed. Fig. 6 shows the TEM images and XRD patterns of the samples prepared at certain reaction time at 180 ^{o}C. The morphology of the products was strongly influenced by reaction time while the phase almost did not change. Fig. 6(a) clearly shows that, after reaction for 8 h, tiny nanoparticle appeared but agglomerated. By further elongating reaction time to 24 h, as shown in Fig. 6(b); the synthesized samples were uniformly dispersed nanoparticles which were similar as the morphology for 12 h in Fig. 3(a). So we selected 12 h as reaction time in our system. In short, reaction time has a small influence on the phase of the sample, but a great influence on morphology.

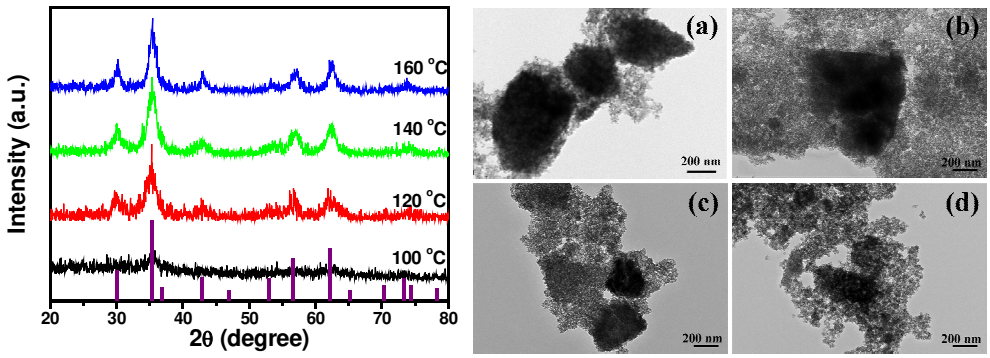

Fig. 7. XRD patterns and TEM images of the samples prepared at different temperature: (a) 100 ^{o}C, (b) 120 ^{o}C, (c) 140 ^{o}C and (d) 160 ^{o}C. The vertical line is the standard pattern of $ZnFe_2O_4$ (JCPDS 22-1012).

The influence of reaction temperature has also been investigated. The XRD patterns and TEM images of the samples prepared at different reaction temperature are shown in Fig. 7. The main peaks of XRD patterns were all indexed to $ZnFe_2O_4$ (JCPDS 22-1012). With the increase of temperature, diffraction intensity of the synthesized samples was strengthened, while the morphology underwent to evolve from shuttle-like to well-dispersed nanoparticles. When the samples were prepared at 100 ^oC, the edge of the shuttle-like morphology was corroded, and with increased temperature, the shuttle-like morphology was destroyed and dispersed gradually. Therefore, the high reaction temperature is beneficial to crystallization and dispersity of as-synthesized samples.

3.2 Gas-sensing properties

To understand the properties of the synthesized $ZnFe_2O_4$ nanoparticles in typical condition, gas-sensing experiments are performed.

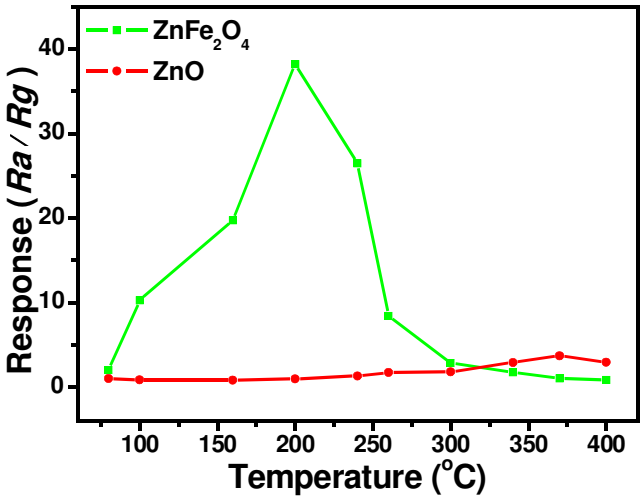

Fig. 8. Responses of sensors based on ZnO and $ZnFe_2O_4$ to acetone gas (500 ppm) versus operating temperatures

It is well known that the response of a semiconductor gas sensor is highly

influenced by its operating temperature. To determine the optimum working temperature, the responses of sensors based on ZnO and $ZnFe_2O_4$ to acetone were examined as a function of temperature, as shown in Fig. 8. The results presented that ZnO-based sensor had weak response to acetone and the response value reached maximum at 370 ^oC in the range from room temperature to 400 ^oC, while the sensor based on $ZnFe_2O_4$ showed good response to acetone, and it reached maximum response value at optimum working temperature of 200 ^oC. So 200 ^oC was selected as optimum working temperatures for the further investigations of sensing performance of as-fabricated sensors.

In the range of test temperatures, the response value first increase with the increasing working temperature and then decrease with further increasing temperature. At a low operating temperature, the gas molecules do not have enough thermal energy to react with surface adsorbed oxygen species O^{2-}, so the reaction rate between target gas and O^{2-} is essentially low. The enhanced response with the increasing temperature can be attributed to two facts. On one hand, the thermal energy obtained is high enough to overcome activation energy barrier of surface reaction; on the other hand, the adsorbed oxygen species convert from O_2 to O^- at elevated temperatures, and thus an increase in electron concentration results in the sensing reaction of a test gas and O^- [39]. Moreover, the reduction in response after maximum is due to the difficulty in exothermic gas adsorption on the surface of electrode at higher temperatures. Therefore, to obtain a high response, an optimum working temperature should be considered.

When $ZnFe_2O_4$ materials meet acetone, the possible reactions are summarized as follows:

$$O_2 + e^- \rightarrow O_2^- \quad (1)$$

$$O_2^- + e^- \rightarrow 2O^- \quad (2)$$

$$C_3H_6O + 8O^- \rightarrow 3CO_2 \uparrow + 3H_2O + 8e^- \quad (3)$$

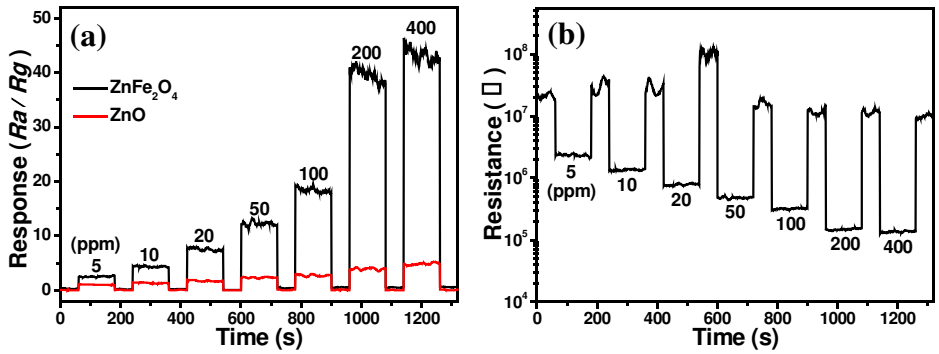

Fig. 9. (a) Real-time response curves of sensors based on ZnO and $ZnFe_2O_4$ nanomaterials and (b) the actual sensor resistance values of $ZnFe_2O_4$ nanoparticles for different acetone concentrations at 200 ^oC.

Fig. 9a shows real-time response curves of the sensors based on precursor ZnO and as-synthesized $ZnFe_2O_4$ nanomaterials upon exposure to different concentrations of acetone between 5 and 400 ppm at optimum working temperature of 200 ^oC. It can be observed that the response value of both sensors increased with gas concentration. And it is worth noting that the response value of $ZnFe_2O_4$-based sensor to acetone was higher than that of ZnO-based sensor. As confirmed by TEM observations, $ZnFe_2O_4$ had smaller size than ZnO, which was beneficial to the improvement of gas sensing property. Moreover, the gas sensing property also depended on surface area of oxide semiconductor. The BET surface of $ZnFe_2O_4$ (115.6 m^2g^{-1}) was higher than that of ZnO (11.54 m^2g^{-1}). A higher surface area can adsorb more molecules, provide available surface reaction sites, thus results in a higher response [36,40]. Therefore,

as-prepared $ZnFe_2O_4$-based sensor has enhanced sensing performance to acetone comparing with precursor ZnO-based sensor. Moreover, Fig. 9b shows the actual resistance values of $ZnFe_2O_4$ nanoparticles for different acetone concentrations at 200 ^oC. The resistance values in air are not too high as compared with the reported works [41,42].

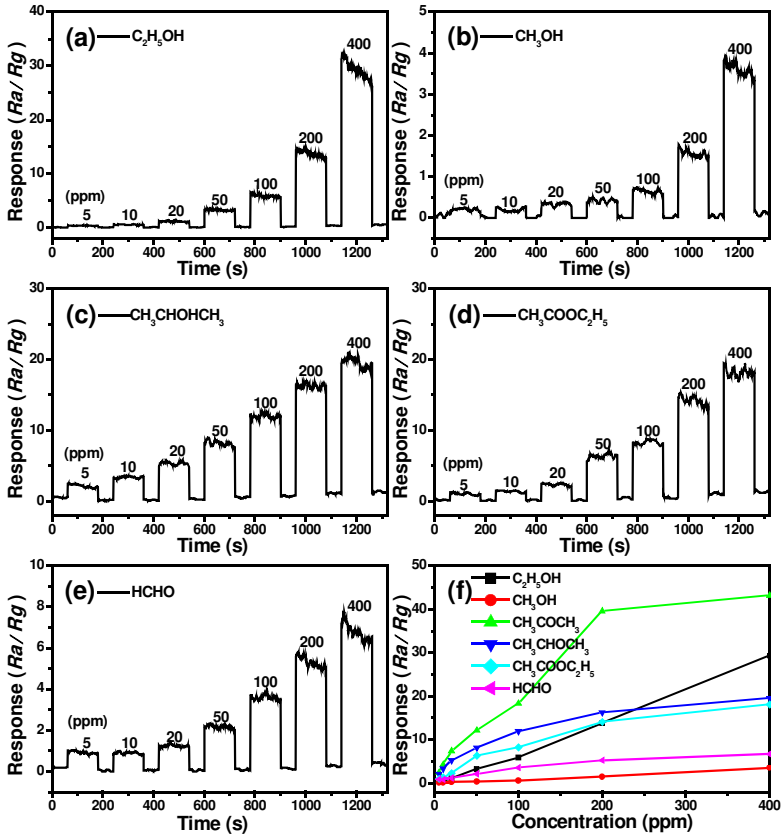

Fig. 10. Real-time response curves of $ZnFe_2O_4$ sensor to several common gases: (a) C_2H_5OH, (b) CH_3OH, (c) $CH_3CHOHCH_3$, (d) $CH_3COOC_2H_5$ and (e) HCHO with different gas concentrations. (f) Relationship curves of response and gas concentrations for different compounds.

Other common compounds, such as ethanol, methanol, isopropanol, ethyl acetate and methanal were also used to evaluate the gas sensing performances of as-synthesized $ZnFe_2O_4$ nanopartilcles. Fig. 10(a-e) shows the curves of responses to different gases between 5 to 400 ppm at working temperature of 200 ^oC. It can be

observed that the response values increased with an increase of gas concentration for different gases, in spite of their own increasing trends. The correlation between the response and gas concentrations for different compounds is shown in Fig. 10(f). It was found that the sensor exhibited higher response to acetone than that of other compounds at the same condition. The results reflected that $ZnFe_2O_4$-based sensors had good selectivity for acetone in the concentration range from 20 to 200 ppm. The response value of $ZnFe_2O_4$-based sensor was 39.5 for 200 ppm acetone gas at 200 ^oC, which was higher than the previous reports [18] [35-38].

4. Conclusions

In summary, $ZnFe_2O_4$ nanoparticles with diameter of ca. 10 nm have been successfully prepared through a facile, effective and scalable hydrothermal method. The magnetization saturation value was relatively as high as 59.0 emu g^{-1}. Based on BET result, the specific surface area of nanoparticles was evaluated to be 115.6 $m^2 g^{-1}$. The reaction conditions, such as the reactant mole ratio, reaction temperature and time played key roles on the phase and morphology of as-prepared products. This synthetic method can be extended to prepare different multifunctional nanomaterials. The gas sensing experiment presented that the synthesized $ZnFe_2O_4$ nanoparticles showed enhanced gas sensing property for acetone than precursor ZnO. $ZnFe_2O_4$-based sensor also showed remarkable selectivity to acetone at relative low working temperature via comparing sensing property to ethanol, methanol, acetone, isopropanol, ethyl acetate and methanal. The results suggested that the synthesized $ZnFe_2O_4$ nanoparticles could

be a potential candidate material for detection of acetone gas.

Acknowledgements

This work is supported by the National Science Foundation of China (NSFC) (Grants 21471001, 21275006), and Natural Science Foundation of Anhui Province (Grant no.1508085MB22), Financed by the 211 Project of Anhui University, and The Key Laboratory of Environment Friendly Polymer Materials of Anhui Province.

References

[1] H. Zhang, C.X. Zhai, J.B. Wu, X.Y. Ma, D.R. Yang, Cobalt ferrite nanorings: Ostwald ripening dictated synthesis and magnetic properties, Chem. Commun. (2008) 5648-5650.

[2] K. Arshak, E. Moore, C. Cunniffe, M. Nicholson, A. Arshak, Preparation and characterization of $ZnFe_2O_4$/ZnO polymer nanocomposite sensors for the detection of alcohol vapours, Superlattices Microstruct. 42 (2007) 479-488.

[3] S.H. Sun, H. Zeng, D.B. Robinson, S. Raoux, P.M. Rice, S.X. Wang, G.X. Li, Monodisperse MFe_2O_4 (M = Fe, Co, Mn) Nanoparticles, J. Am. Chem. Soc. 126 (2004) 273-279.

[4] H.L. Zhu, X.Y. Gu, D.T. Zuo, Z.K. Wang, N.Y. Wang, K.H. Yao, Microemulsion-based synthesis of porous zinc ferrite nanorods and its application in a room-temperature ethanol sensor, Nanotechnology 19 (2008) 405503.

[5] Y.S. Fu, X. Wang, Magnetically Separable $ZnFe_2O_4$-Graphene Catalyst and its High Photocatalytic Performance under Visible Light Irrdiation, Ind. Eng. Chem. Res. 50 (2011) 7210-7218.

[6] J. Li, A.R. Wang, Y.Q. Lin, X.D. Liu, J. Fu, L.H. Lin, A study of $ZnFe_2O_4$ nanoparticles modified by ferric nitrate, J. Magn. Magn. Mater. 330 (2013) 96-100.

[7] N.N. Wang, H.Y. Xu, L. Chen, X. Gu, J. Yang, Y.T. Qian, A general approach for MFe_2O_4 (M = Zn, Co, Ni) nanorods and their high performance as anode materials for lithium ion batteries, J. Power Sources 247 (2014) 163-169.

[8] Z.M. Li, X.Y. Lai, H. Wang, D. Mao, C.J. Xing, D. Wang, General Synthesis of Homogeneous Hollow Core-Shell Ferrite Microspheres, J. Phys. Chem. C. 113 (2009) 2792-2797.

[9] F.F. Liu, X.Y. Li, Q.D. Zhao, Y. Hou, X. Quan, G.H. Chen, Structural and photovoltaic properties of highly ordered $ZnFe_2O_4$ nanotube arrays fabricated by a facile sol-gel template method, Acta mater. 57 (2009) 2684-2690.

[10] A. Sutka, J. Zavickis, G. Mezinskisa, D. Jakovlevs, J. Barloti, Ethanol monitoring by $ZnFe_2O_4$ thin film obtained by spray pyrolysis, Sens. Actuators, B 176 (2013) 330-334.

[11] Y. Kido, K. Nakanishi, K. Kanamori, Sol-gel synthesis of zinc ferrite-based xerogel monoliths with well-defined macropores, RSC Adv. 3 (2013) 3661-3666.

[12] S.L. Darshane, R.G. Deshmukh, S.S. Suryavanshi, I.S. Mulla, Gas-Sensing Properties of Zinc Ferrite Nanoparticles Synthesized by the Molten-Salt Route, J. Am. Ceram. Soc. 91 (8) (2008) 2724-2726.

[13] M.M. Rahman, S.B. Khan, M. Faisal, A.M. Asiri, K.A. Alamry, Highly sensitive

formaldehyde chemical sensor based on hydrothermally prepared spinel $ZnFe_2O_4$ nanorods, Sens. Actuators, B 171-172 (2012) 932-937.

[14] H. Xia, Y.Y. Qian, Y.S. Fu, X. Wang, Graphene anchored with $ZnFe_2O_4$ nanoparticles as a high-capacity anode material for lithium-ion batteries, Solid State Sci. 17 (2013) 67-71.

[15] F. Mueller, D. Bresser, E. Paillard, M. Winter, S. Passerini, Influence of the carbonaceous conductive network on the electrochemical performance of $ZnFe_2O_4$ nanoparticles, J. Power Sources 236 (2013) 87-94.

[16] Y.Y. Sun, W.Z. Wang, L. Zhang, S.M. Sun, E.P. Gao, Magnetic $ZnFe_2O_4$ octahedra: Synthesis and visible light induced photocatalytic activities, Mater. Lett. 98 (2013) 124-127.

[17] G.Y. Zhang, C.S. Li, F.Y. Cheng, J. Chen, $ZnFe_2O_4$ tubes: Synthesis and application to gas sensors with high sensitivity and low-energy consumption, Sens. Actuators, B 120 (2007) 403-410.

[18] J.Y. Patil, D.Y. Nadargi, J.L. Gurav, I.S. Mulla, S.S. Suryavanshi, Glycine combusted $ZnFe_2O_4$ gas sensor: Evaluation of structural, morphological and gas response properties, Ceram. Int. 40 (2014) 10607-10613.

[19] Y.L. Cao, D.Z. Jia, P.F. Hu, R.Y. Wang, One-step room-temperature solid-phase synthesis of $ZnFe_2O_4$ nanomaterials and its excellent gas-sensing property, Ceram. Int. 39 (2013) 2989-2994.

[20] J.M. Song, J. Zhang, J.J. Ni, H.L. Niu, C.J. Mao, S.Y. Zhang, Y.H. Shen, One-pot synthesis of ZnO decorated with AgBr nanoparticles and its enhanced photocatalytic properties, CrystEngComm 16 (2014) 2652-2659.

[21] J.Q. Wan, X.H. Jiang, H. Li, K.Z. Chen, Facile synthesis of zinc ferrite nanoparticles as non-lanthanide T_1 MRI contrast agents, J. Mater. Chem. 22 (2012) 13500-13505.

[22] M.Y. Wang, L. Sun, J.H. Cai, P. Huang, Y.F. Su, C.J. Lin, A facile hydrothermal deposition of $ZnFe_2O_4$ nanoparticles on TiO_2 nanotube arrays for enhanced visible light photocatalytic activity, J. Mater. Chem. 1 (2013) 12082-12087.

[23] M.S. Xue, S. Wang, K.H. Wu, J.D. Guo, Q.L. Guo, Surface Structural Evolution in Iron Oxide Thin Files, Langnuir 27 (1) (2011) 11-14.

[24] L. Sun, R. Shao, L.Q. Tang, Z.D. Chen, Synthesis of $ZnFe_2O_4$/ZnO nanocomposites immobilized on graphene with enhanced photocatalytic activity under solar light irradiation, J. Alloys. Compd. 564 (2013) 55-62.

[25] T. Yamashita, P. Hayes, Analysis of XPS spectra of Fe^{2+} and Fe^{3+} ions in oxide materials, Appl. Surf. Sci. 254 (2008) 2441-2449.

[26] P.Z. Guo, L.J. Cui, Y.Q. Wang, M. Lv, B.Y. Wang, X.S. Zhao, Facile Synthesis of $ZnFe_2O_4$ Nanoparticles with Tunable Magnetic and Sensing Properties, Langmuir 29 (2013) 8997-9003.

[27] H.H. Kou, L.P. Jia, C.M. Wang, Electrochemical deposition of flower-like ZnO nanoparticles on a silver-modified carbon nanotube/polyimide membrane to improve its photoelectric activity and photocatalytic performance, Carbon. 50 (2012) 3522-3529.

[28] Y. Hou, X.Y. Li, Q.D. Zhao, G.H. Chen, $ZnFe_2O_4$ multi-porous microbricks/graphene hybrid photocatalyst: Facile synthesis, improved activity and photocatalytic mechanism, Appl. Catal., B 142-143 (2013) 80-88.

[29] H.J. Lv, L. Ma, P. Zeng, D.N. Ke, T.Y. Peng, Synthesis of floriated $ZnFe_2O_4$ with porous nanorod structures and its photocatalytic hydrogen production under visible light, J. Mater.

Chem. 20 (2010) 3665-3672.
[30] Z.D. Nan, X. Xue, W.G. Hou, X. Yan, S.H. Han, Fabrication of MCM-41 mesoporous silica through the self-assembly supermolecule of β-CD and CTAB, J. Solid State Chem. 180 (2007) 780-784.
[31] H.Y. Liu, Y.P. Guo, Y.Y. Zhang, F. Wu, Y. Liu, D. Zhang, Synthesis and properties of $ZnFe_2O_4$ replica with biological hierarchical structure, Mater. Sci. Eng., B 178 (2013) 1057-1061.
[32] C.B.R. Jesus, E.C. Mendonca, L.S. Silva, W.S.D. Folly, C.T. Meneses, J.G.S. Duque, Weak ferromagnetic component on the bulk $ZnFe_2O_4$ compound, J. Magn. Magn. Mater. 350 (2014) 47-49.
[33] Z.P. Chen, W.Q. Fang, B. Zhang, H.G. Yang, High-yield synthesis and magnetic properties of $ZnFe_2O_4$ single crystal nanocubes in aqueous solution, J. Alloys. Compd. 550 (2013) 348-352.
[34] J.M. Song, S.S. Zhang, S.H. Yu, Multifunctional $Co_{0.85}Se$-Fe_3O_4 Nanocomposites: Controlled Synthesis and Their Enhanced Performances for Efficient Hydrogenation of *p*-Nitrophenol and Adsorbents, Small 10 (2014) 717-724.
[35] L.P. Qin, J.Q. Xu, X.W. Dong, Q.Y. Pan, Z.X. Cheng, Q. Xiang, F. Li, The template-free synthesis of square-shaped SnO_2 nanowires: the temperature effect and acetone gas sensors, Nanotechnology 19 (2008) 185705.
[36] M.R. Alenezi, S.J. Henley, N.G. Emerson, S.P. Silva, From 1D and 2D nanostructures to 3D hierarchical structures with enhanced gas sensing properties, Nanoscale 6 (2014) 235-247.
[37] Z. Zhang, X.L. Li, H.M. Ji, Y.G. Zhou, Preparation and acetone sensitive characteristics of nano-crystalline $ZnFe_2O_4$ thin films, Mater. Sci. Technology 18 (2010) 23-26.
[38] F. Liu, X.F. Chu, Y.P. Dong, W.B. Zhang, W.Q. Sun, L.M. Shen, Acetone gas sensors based on grapheme-$ZnFe_2O_4$ composite prepared by solvothermal method, Sens. Actuators, B 188 (2013) 469-474.
[39] J. Chen, J. Li, J.H. Li, G.Q. Xiao, X.F. Yang, Large-scale syntheses of uniform ZnO nanorods and ethanol gas sensors application, J. Alloys. Compd. 509 (2011) 740-743.
[40] S.Y. Liu, L.Zhou, L.Y. Yao, L.Y. Chai, L. Li, G. Zhang, K. Kan, K.Y. Shi, One-pot reflux method sunthesis of cobalt hydroxide nanoflake-reduced graphene oxide hybrid and their No_x gas sensors at romm temperature, J. Alloys. Compd. 612 (2014) 126-133.
[41] K. Inyawilert, A. Wisitaoraat, C. Sriprachaubwong, A. Tuantranont, S. Phanichphant, C. Liewhiran, Rapid ethanol sensor based on electrolytically-exfoliated grapheme-loaded flame-made In-doped SnO_2 composite film, Sens. Actuators, B 209 (2015) 40-55.
[42] C. Baratto, R. Kumar, G. Faglia, K. Vojisavljevic, B. Malic, p-Type copper aluminum oxide thin films for gas-sensing applications, Sens. Actuators, B 209 (2015) 287-296.

Author Biographies

Jie Zhang received her bachelor's degree in Department of Chemistry, Huangshan University in 2012. She is currently pursuing MS Degree at Anhui University. Her reseach interests are the synthesis of inorganic nanomaterials and their applications in photocatalysis and gas sensors.

Ji-Ming Song received his PhD degree in inorganic chemistry from University of Science and Technology of China in 2007, and worked as a postdoctoral researcher in Hefei National Laboratory for Physical Sciences at the Microscale from June, 2007 to May, 2009. He worked in Carnegie Mellon Unversity as a visiting scholar from November, 2013 to November, 2014. Currently he is a professor of Anhui University. His research fields are the synthesis, assembly, characterization and applications of nanomaterials.

He-Lin Niu received his PhD degree in University of Science and Technology of China in 2004. Then he worked in Hefei National Laboratory for Physical Sciences at the Microscale and Korea University as a post doc fellow one after another. Currently, he is a professor of Anhui University. His current research interest is in material chemistry and nanosciences.

Chang-Jie Mao received his PhD degree in Nanjing University in 2008. He studied in Case Western Reserve University as a joint-supervision doctoral student from January, 2007 to January, 2008. Now he is working at the Chemistry and Chemical Engineering in Anhui University as an associate professor. His research interests are analytic electrochemistry and biosensor.

Sheng-Yi Zhang received his PhD degree in Nanjing University in 2006. Currently he is a professor of Anhui University. His research interests are electrochemistry and synthesis of nanomaterials.

Yu-Hua Shen graduated from AnQing Normal University in 1982. Now she is a professor of Anhui University. Her research fields are biological mineralization and inorganic chemistry.